

Optimizing the precision of infrared measurements using the Eppley Laboratory, Inc. model PIR pyrgeometer

Joseph J. Michalsky¹, John A. Augustine¹, Emiel Hall¹, and Benjamin R. Sheffer^{1, 2}

¹Global Monitoring Laboratory, National Oceanic and Atmospheric Administration, Boulder, Colorado 80305, USA

²Cooperative Institute for Research in Environmental Sciences, University of Colorado, Boulder, Colorado 80309, USA

Correspondence: Joseph Michalsky (joseph.michalsky@noaa.gov)

Abstract. The Eppley Precision Infrared Radiometer (PIR) is widely used for broadband (3.5-50 μm), thermal infrared wavelength measurements of the downwelling and upwelling radiation from the atmosphere and surface, respectively. The field of view of the instrument is 2π steradians with a receiver that has an approximate cosine response. In this paper we examine four equations suggested by the literature that have been used to transfer irradiance calibrations from our standard PIRs that are calibrated at the World Radiation Center to field units used for network operations. We first discuss various equations used to convert the resistance measurements of the thermistors to temperatures of the body and dome that are used in the derivation of incoming irradiance. We then use the four related, but distinct, equations for the transfer of the calibration from standard PIRs to field instruments. A clear choice for the preferred equation to use for calibration and transfer of calibration to field PIRs emerges from this study.

1. Introduction

The Eppley Precision Infrared Radiometer (PIR) is a pyrgeometer developed to measure broadband (3.5-50 μm) thermal infrared (hereafter, IR) radiation emitted by the atmosphere and surface. Detecting even small changes in atmospheric and surface IR in the environment are important to understand as they may indicate temperature changes in the environment caused by changes in the atmospheric composition or cloud cover.

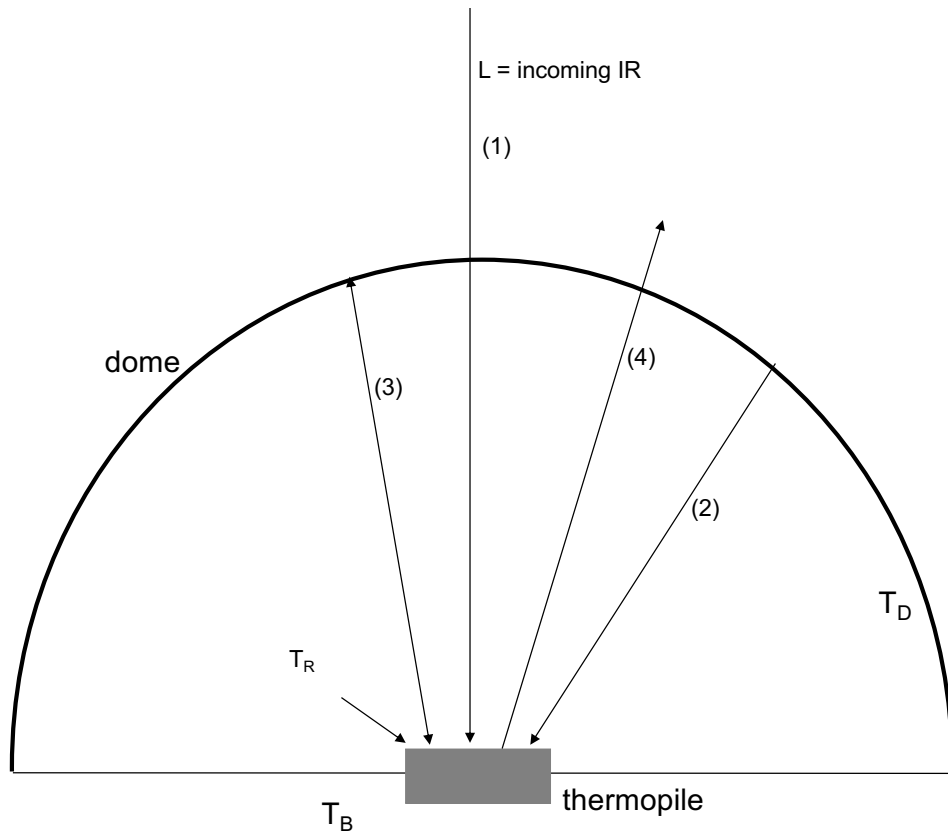
The PIR originally came equipped with a battery-powered circuit to compensate for the radiation emitted by the body so the net signal from the instrument was a measure of actual incoming IR radiation. Users of this instrument that are interested in the optimum precision in their IR measurements do not use the battery-powered circuit, but, instead, use temperatures from two thermistors connected to the body and dome of the instrument along with the thermopile output to calculate the incoming IR irradiance signal.

Fig. 1 illustrates the most significant incoming and outgoing IR irradiances at the thermopile surface. To derive L , the incoming IR radiation from the hemisphere outside the instrument,

45 radiative equilibrium of the instrument must be defined. To do that, the sum of the incoming
 46 radiation transmitted through the dome (labeled 1), radiation emitted by the dome to the receiver
 47 (labeled 2), and the radiation emitted by the thermopile surface and reflected by the dome
 48 (labeled 3) are set equal to the radiation emitted by the thermopile surface (labeled 4, which is
 49 the largest of the IR signals). Note that the dome transmits IR radiation between 3.5 and 50 μm ,
 50 however, the transmission is not perfect, nor uniform. Considering these components Albrecht
 51 and Cox (1977) formulated Eq. (1) for the externally received radiation as
 52

$$L = U_{thermopile}(c_1 + c_2 T_B^3) + \epsilon_o \sigma T_B^4 - k\sigma(T_D^4 - T_B^4), \quad (1)$$

53 where $U_{thermopile}$ is the voltage measured across the thermopile, T_B and T_D are the body and dome
 54 temperatures in K, σ is the Stefan-Boltzmann constant, ϵ_o is the emissivity of the detector, and
 55 c_1 , c_2 , and k are constants to be determined in calibration.
 56



57 **Figure 1.** Schematic for the most significant incoming and outgoing IR radiation components on
 58 the thermopile surface (numbered 1 – 4) that are considered in calculating the incident
 59 atmospheric IR irradiance. The top of the dark rectangle is the receiving surface surrounded by
 60 the dome that transmits IR in the range 3-50 μm . YSI 44031 thermistors are used to measure T_B
 61 of the body (thermistor buried in the brass body of the PIR) and T_D of the dome in K. T_R is the
 62 estimated receiver temperature in K.
 63
 64

65 In practice Albrecht and Cox (1977) dropped the $c_2 T_B^3$ term as negligible relative to the c_1 term
 66 and set the emissivity of the body of the instrument ϵ_0 to 1 yielding this commonly expressed
 67 form of their equation
 68

$$L = \frac{U_{thermopile}}{C} + \sigma T_B^4 - k\sigma(T_D^4 - T_B^4), \quad (2)$$

69
 70 where c_1 has been replaced by $1/C$.
 71

72 Philipona et al. (1995), however, used Eq. (1) in its entirety, but to compare symbolically to Eq.
 73 (2) it is written
 74
 75

$$L = \frac{U_{thermopile}}{C} (1 + k_1 \sigma T_B^3) + k_2 \sigma T_B^4 - k_3 \sigma (T_D^4 - T_B^4), \quad (3)$$

76 where the T_B^3 term in Eq. (1) is retained, the emissivity of the body is k_2 , and k_3 is the same as k
 77 in Eq. (2). All constants, C , k_1 , k_2 , and k_3 , are determined in calibration.
 78
 79
 80

81 Payne and Anderson (1999) used the functional form of Eq. (2), but substituted T_R for the T_B ,
 82 where T_R is the empirically calculated approximate temperature of the receiving surface rather
 83 than the measured body temperature as illustrated in Fig. 1. Thus,
 84

$$L = \frac{U_{thermopile}}{C} + \sigma T_R^4 - k\sigma(T_D^4 - T_R^4). \quad (4)$$

85
 86 Payne and Anderson (1999) estimated T_R using Eq. 5
 87

$$T_R = T_B + 0.694 \cdot U_{thermopile} \quad (5)$$

88 where $U_{thermopile}$ is in millivolts, and the emissivity ϵ_0 is set to unity.
 89
 90

91 Reda et al. (2002) used a form similar to Eq. (4)
 92

$$L = k_0 + \frac{U_{thermopile}}{C} + k_2 \sigma T_R^4 - k_3 \sigma (T_D^4 - T_R^4), \quad (6)$$

93 where the instrument body emissivity k_2 is derived during calibration and a constant term k_0 is
 94 introduced. T_R is nearly the same as Eq. (5) with 0.704 replacing the constant 0.694. In this paper
 95 we drop the constant term k_0 since there is no physical justification for including it.
 96
 97

98 Since there are four versions of the original Albrecht and Cox (1977) Eq. (1), this paper attempts
 99 to determine which version is best, in the precision sense, to use for PIR calibration transfer, and
 100 general use in converting PIR measured quantities to physical units. The organization of this
 101 paper is as follows. Because accurate internal thermistor temperatures are critical to pyrgeometer

102 IR measurements, we first examine various versions of the standard cubic equation used to
 103 convert the YSI 44031 thermistor resistance to the temperatures of the PIR body and dome. We
 104 then calibrate six test PIRs by transferring the calibrations of our three standard PIRs that were in
 105 turn calibrated at the World Radiation Center (WRC) in Davos, Switzerland, using the World
 106 Infrared Standard Group (WISG). Comparisons are then made between the mean irradiance of
 107 the three standard PIRs and the computed irradiance from the test PIRs using the four different
 108 forms of the original Albrecht and Cox (1977) formula, i.e., Eq. (1) to calibrate each. Boxplots
 109 are used to demonstrate the level of agreement between the standard PIRs and test PIRs for the
 110 various formulations. Lastly, a clear conclusion with regards to the preferred technique to use for
 111 calibrations and field measurements is suggested.

112

113

114 2. PIR Temperature Measurements

115

116 The body and dome temperatures in the Eppley PIR pyrgeometer are measured using the YSI
 117 44031 thermistor. The YSI company provided a table of resistance versus temperature at one K
 118 resolution. To get a finer resolution, a mathematical fit to the tabulated data is required. Steinhart
 119 and Hart (1968) found that a cubic fit of inverse temperature to the log of measured resistance
 120 matched many of the manufacturer's thermistor data points over a wide temperature range. Their
 121 equation is

122

$$\frac{1}{T} = a + b \cdot \ln(R) + c \cdot (\ln R)^2 + d \cdot (\ln R)^3, \quad (7)$$

123

124 where T is the temperature in K and R is the measured resistance in ohms or kilohms. Note that
 125 in the standard Steinhart-Hart equation, the 'c' is set to zero. Coefficients *a*, *b*, and *d* differ
 126 depending on whether ohms or kilohms are used, and on the temperature range over which the
 127 fit is made.

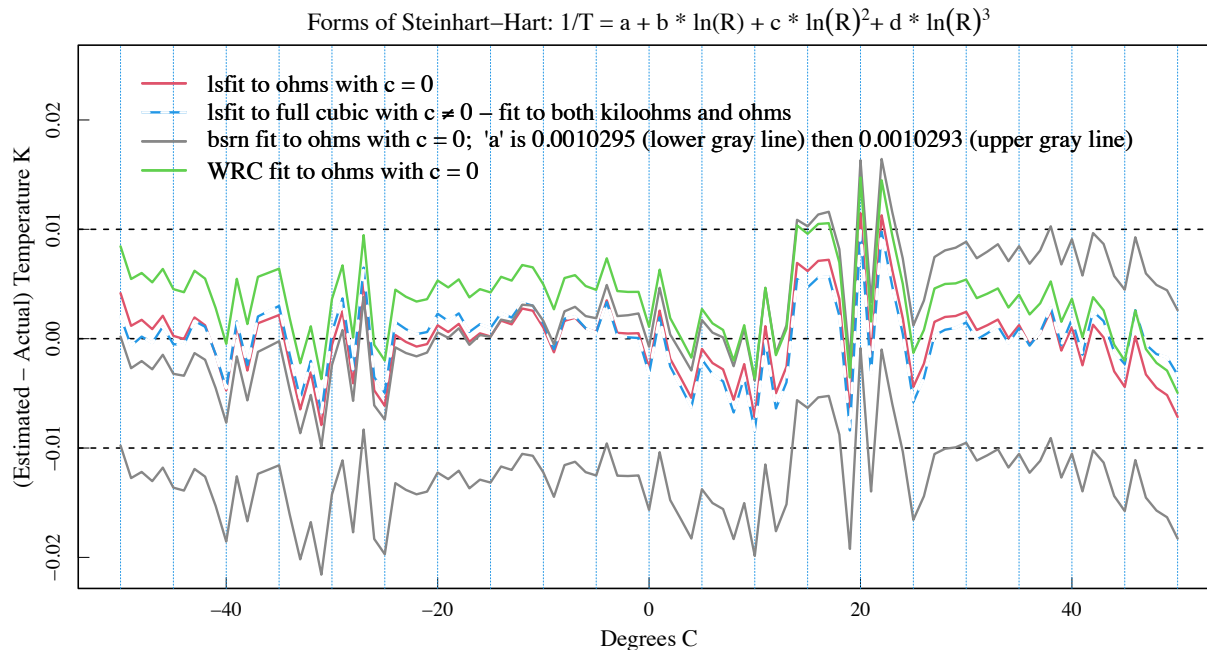
128

129 Fig. 2 is a plot of six independently-derived fits to the same manufacturer's YSI 44031
 130 thermistor data, and the table below lists the coefficients of Eq. 7 for those fits. The y-axis is the
 131 temperature estimate based on the fit minus the tabulated thermistor data to which the fit is
 132 made. The least-squares fit to Eq. (7) (no quadratic term) is indicated by the red line if ohms are
 133 used. If a full cubic relationship, including a quadratic term, is used to fit the tabulated data in
 134 kilohms, then similar, but not identical, agreement to the red line is obtained (blue-white line).
 135 Interestingly, fitting the full cubic relationship to either ohms or kilohms yields identical results
 136 (again, note the blue-white line). This is not the case if the quadratic term is not included in the
 137 fitting to ohms versus kilohms as discussed in the appendix. Two gray fits in Fig. 2 are from the
 138 Baseline Surface Radiation Network (BSRN) - Operation Manual Version 2.1 (McArthur, 2005),
 139 and use YSI 44031 resistance in ohms. That published equation yields the bottom gray curve that
 140 is displaced from the main grouping in Figure 2. If their coefficient *a* is modified slightly from
 141 the published 0.0010295 to 0.0010293, as shown in the legend, then an improved fit (upper gray
 142 curve) is obtained that agrees well with the others. The green curve, used by the World Radiation
 143 Center (WRC) in Davos, Switzerland, was fit over a -30 to +40 °C range, but does well over the
 144 entire range of -50 to 50 °C considered here. Differences among the various fits in Fig. 2 are

145 small. All but the bottom gray fit in Fig. 2 cause less than 0.1 Wm^{-2} of uncertainty in the
 146 irradiance estimate.
 147

	a =	b =	c =	d =
Red (ohms)	0.001029607	0.0002390769	0.0	1.567609E-07
White (ohms)	0.001020630	0.0002416721	-2.47485E-07	1.64547E-07
Blue (kiloohms)	0.002732470	0.0002618082	3.162474E-06	1.645474E-07
Gray (ohms)	0.0010295 Better 0.0010293	0.0002391	0.0	1.568E-07
Magenta (ohms)	0.00102972	0.00023906	0.0	1.5677E-07

148
 149 The larger uncertainty in thermistor temperature measurements is the fundamental accuracy of
 150 the thermistors used in the PIR, which are specified to be replaceable to 0.2 K. At 300 K, a
 151 difference of 0.2 K is a little over 1 Wm^{-2} . In this paper the full cubic (blue-white curve) is used
 152 to compute PIR temperatures in the analyzed data.
 153



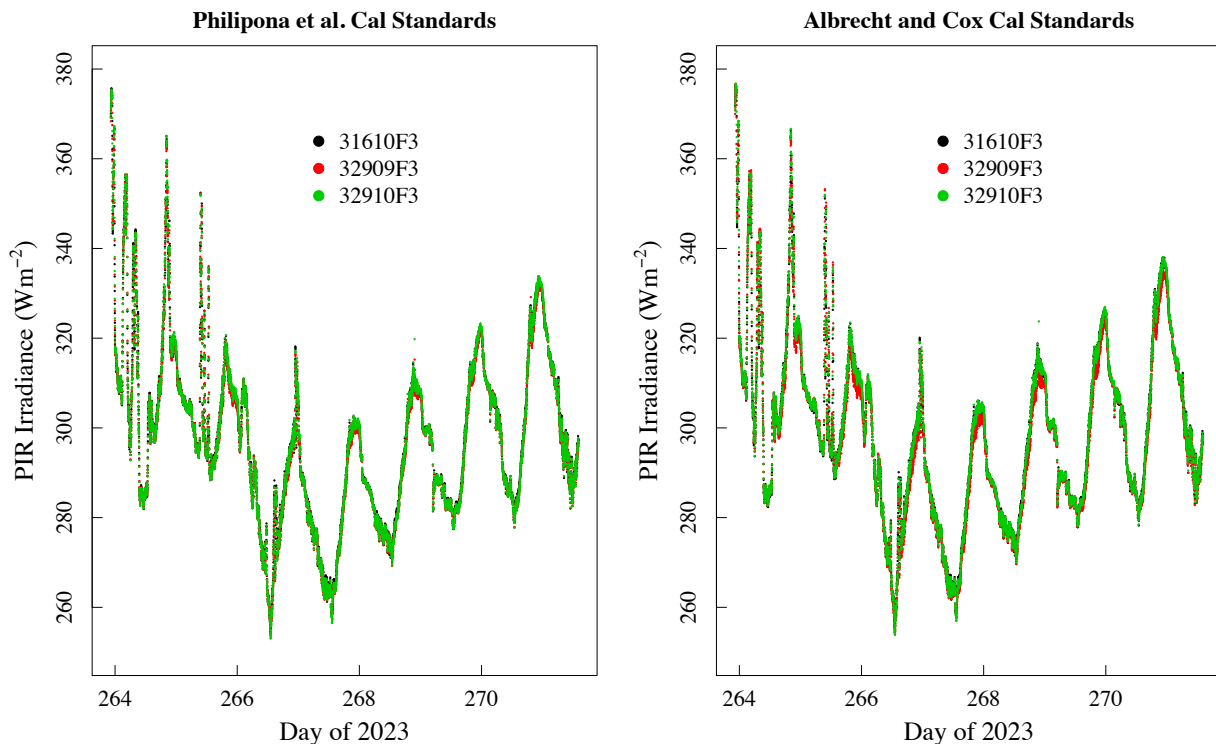
154
 155 **Figure 2.** Six independent fits using forms of Eq. (7) to the YSI 44031 tabulated data after
 156 subtraction of the tabulated data over the range -50 to $50 \text{ }^\circ\text{C}$ in 1°C increments. Similar
 157 agreement among all fits ensues if the small change to the published BSRN constant a is made.
 158 The full cubic fits (blue-white line) overlap whether ohms or kiloohms are used (with different
 159 coefficients, of course).
 160

161 3. Four Methods of PIR Calibration Transfer

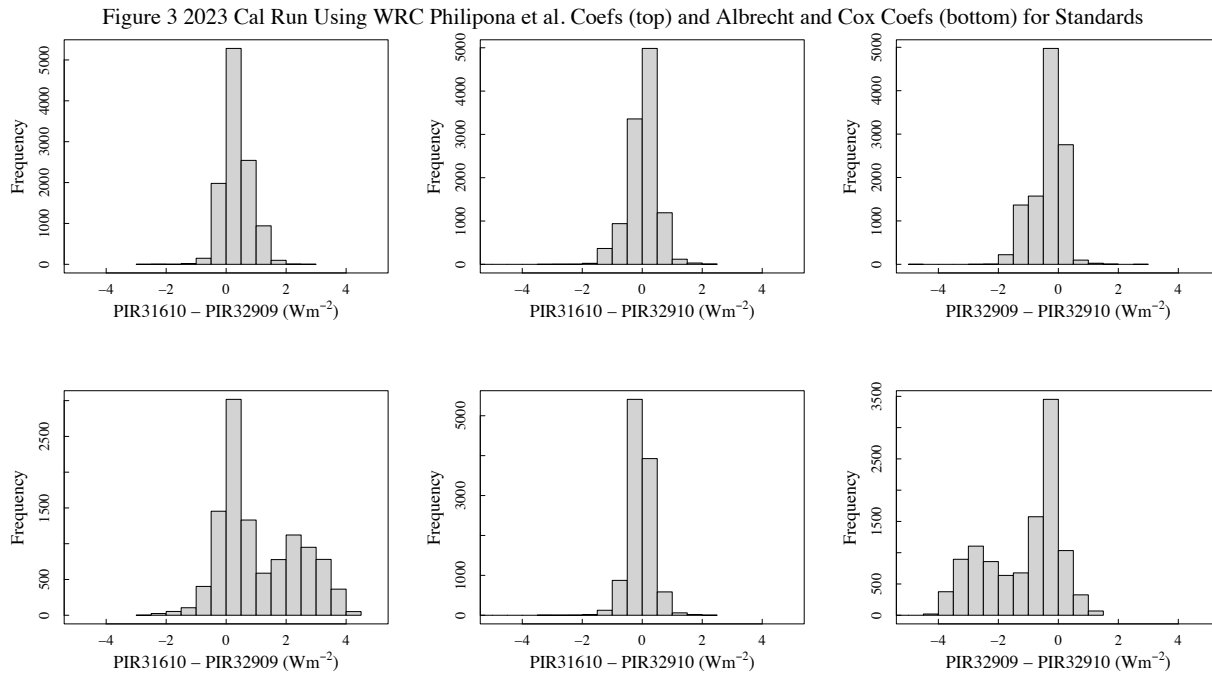
162
 163 In this section, we examine the performance of Eq. (2), (3), (4), and (6) in transferring
 164 calibrations from our three “standard” PIRs to field PIRs. Our standard PIRs were calibrated
 165 against the world reference (<https://www.pmodwrc.ch/en/world-radiation-center-2/irs/wisg/>) in
 166 2018, 2022, and 2024 at the WRC, which is part of the PMOD in Davos, Switzerland. Each

167 standard was returned with two sets of coefficients, one set for Eq. (2) and one set for Eq. (3).
168 The WRC calibration of our standard PIRs uses their blackbody over a range of pyrgeometer and
169 cavity temperatures to determine the k_i 's in Eq. (3). The C determined by this regression is not
170 used, but is set using clear and stable skies outdoors.

171
172 To transfer the standard PIRs' calibration to field radiometers, our WRC-calibrated standard
173 PIRs and test PIRs are arranged side-by-side for a week or more on an outdoor horizontal
174 observing platform, with no significant obstructions surrounding the platform. Note that all
175 calibration coefficients of Eq. (3) for our test PIRs are obtained by regression analysis, i.e., we
176 used no blackbody for calibration transfer. For this paper two calibration periods and three PIRs
177 from each are analyzed. However, all figures for this paper only display results from the 2023
178 calibration performed at Table Mountain near Boulder, Colorado USA. Diurnal variability
179 shown in Fig. 3(a) indicates the type of conditions used for calibration. On the left are the three
180 standard PIR's outputs with the WRC's Philipona et al. (1995) coefficients applied. On the right
181 are the same standard PIR's with the WRC's Albrecht and Cox (1977) coefficients applied.
182 Agreement among the three on the left is very good because the last-plotted PIR readings (green)
183 overplot the first two (black and red). Agreement on the right is nearly as good but with some
184 underestimation by PIR 32909F3 (red dots). Histograms in Fig. 3(b) indicates the degree of
185 agreement among our standard PIRs more clearly with closer agreement among the results using
186 the Philipona et al. (1995) coefficients.
187



188
189 **Figure 3(a).** Calculated IR irradiance from our three standard PIRs (serial numbers in the
190 legend) using Philipona et al. coefficients provided by WRC are overplotted on the left and the
191 Albrecht and Cox coefficients are used on the right. This demonstrates the agreement among the
192 standard PIRs using the two methods. The number of days used is typical for our calibration
193 runs.



195
 196 **Figure 3(b).** Histograms of the differences (Wm^{-2}) among our standard PIRs applying either the
 197 Philipona et al. (1995) WRC-assigned calibration coefficients (top) or the Albrecht and Cox
 198 (1997) WRC-assigned coefficients (bottom). Clearly, there is closer agreement in top row.

199
 200 Before comparing results from Eq. (2), (3), (4), and (6), we first compare results from only
 201 Albrecht and Cox (Eq. 2) and Philipona et al. (Eq. 3) for which the WRC provided both sets of
 202 coefficients. In this test, the mean IR irradiance of the three standard PIRs is compared to
 203 computed IR from a test PIR that was calibrated using the mean of these standard PIRs. The
 204 least-squares fitting technique to determine the calibration coefficients for the test instrument
 205 uses a robust function in the R language (`MASS::rlm`) that de-weights outliers to reduce the
 206 effects of noisy, for example, rain-contaminated, and other outlier data. As we shall discuss in
 207 the final section, this appears to be comparable to the strict criteria used at the WRC for
 208 calibration transfer. However, it should be noted that days with known rain events are removed
 209 from all test data sets before a calibration transfer is attempted.

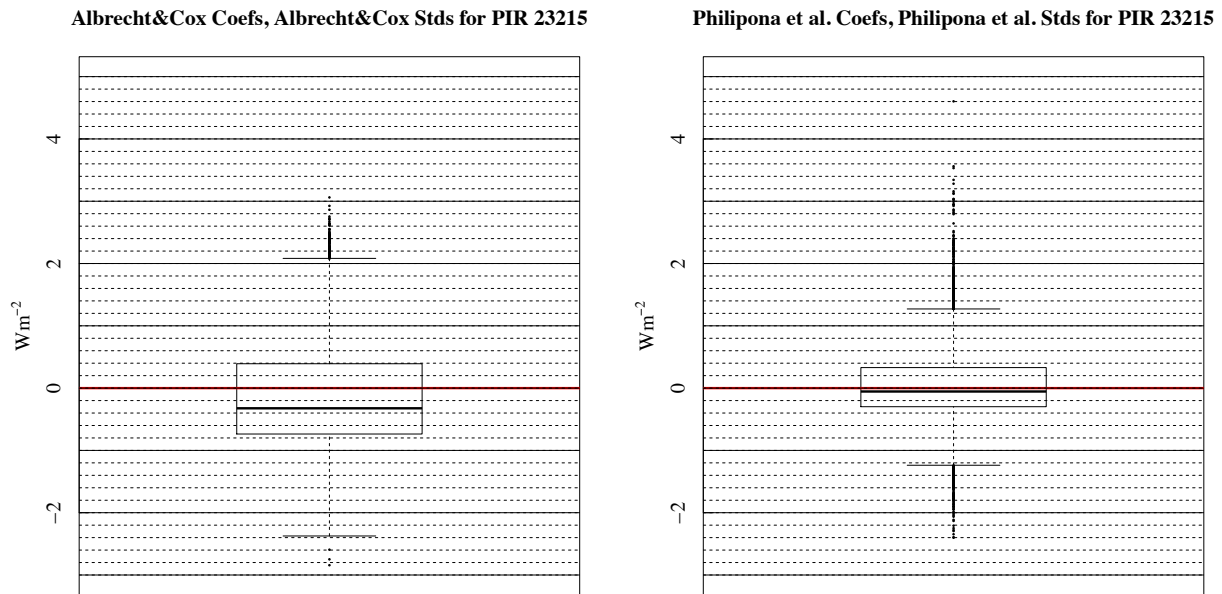
210
 211 In Figure 4, boxplots are used to compare the performance of the two calibration methods
 212 applied to the standard PIRs at the WRC, i.e., Albrecht-and-Cox (1977) and Philipona et al.
 213 (1995). The “box” in these plots contain 50% of the data, and the lines extending from the top
 214 and bottom of the box, or “whiskers,” include about 95% for normally distributed data. In the
 215 top-left panel of Fig. 4 the three standard PIRs use the WRC-provided Albrecht and Cox (1977)
 216 coefficients, and the average of the three standard PIRs is compared to coincident test PIR (SN
 217 23215F3) data, also calculated using Albrecht and Cox (1977). The boxplot summarizes those
 218 differences over the entire calibration period for PIR 23215F3. The boxplot on the top right
 219 summarizes differences following the same procedure, but using Philipona et al. (1995)
 220 coefficients for the standard PIRs (WRC-provided) and for the test PIR. Comparing the top
 221 panels of Fig. 4, the one on the right, where Philipona coefficients are used exclusively, has a

222 smaller box, shorter whiskers, and a median nearer to zero compared to the panel on the left
223 where Albrecht and Cox was used exclusively.

224

225 The bottom panels of Fig. 4 show the same comparison for a different test PIR (SN 38805F3).
226 The same comments apply, with the Philipona et al. (1995) calibrated data (bottom right) giving
227 smaller spread in the box and whiskers, and the median nearer zero, while there is more spread in
228 the bottom-left panel where Albrecht and Cox (1977) is used. Differences in the lower panels of
229 Fig. 4 are generally greater than those in the top panels. The calibration data for these two test
230 instruments were collected concurrently, which suggests that the disparity arises from inherent
231 characteristics of the instruments themselves. We studied a total of six instruments from two
232 distinct calibration periods in this way and found that in every case using the Philipona et al.
233 (1995) form (Eq. 3) gave better results than the formulation of Albrecht and Cox (1977) (Eq.
234 (2)).

235

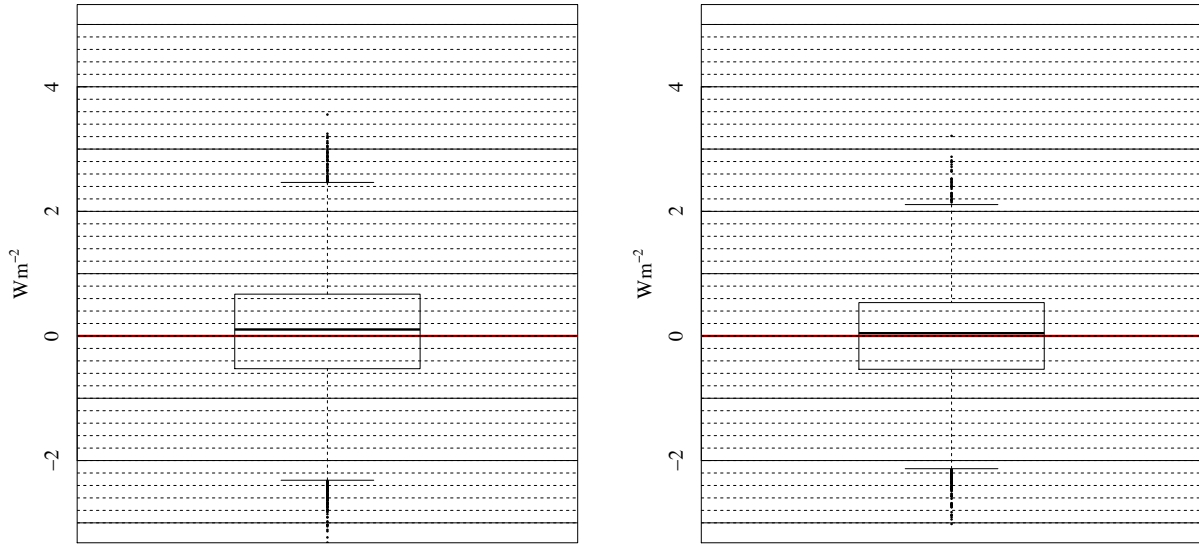


236

237

Albrecht&Cox Coefs, Albrecht&Cox Stds for PIR 38805

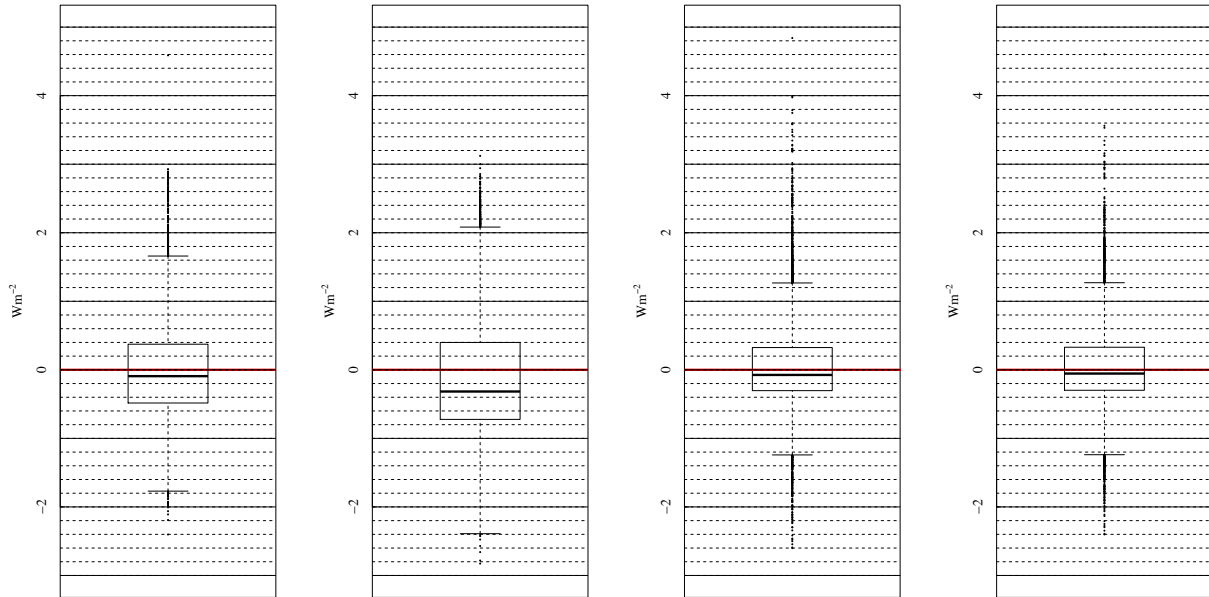
Philipona et al. Coefs, Philipona et al. Stds for PIR 38805



238
239 **Figure 4.** (top) Boxplots of the differences between applying Albrecht and Cox (1977)
240 calibrations and applying Philipona et al. (1995) calibrations for PIR 23215. Note the differences
241 in box widths, whisker lengths, and median values. (bottom) Boxplots for a different PIR
242 (38805) that was calibrated at the same time as the one in Fig. 4 (top).
243
244
245

246 Next, we compare results from all four equations (2), (3), (4), and (6) for the same two PIRs as in
247 Fig. 4. Since Fig. 4 suggests that the Philipona et al. (1995) Eq. (3) produces better results than
248 Albrecht and Cox (1977) Eq. (2), we use Philipona et al. (1995) coefficients provided by WRC
249 to compute IR irradiance for the standard PIRs and average these as “truth” for all of the
250 comparisons. For both test PIRs in Fig. 5 (top and bottom) the last boxplot on the right
251 (Philipona et al., 1995) gives the best results followed by the adjacent boxplot (Reda).
252
253

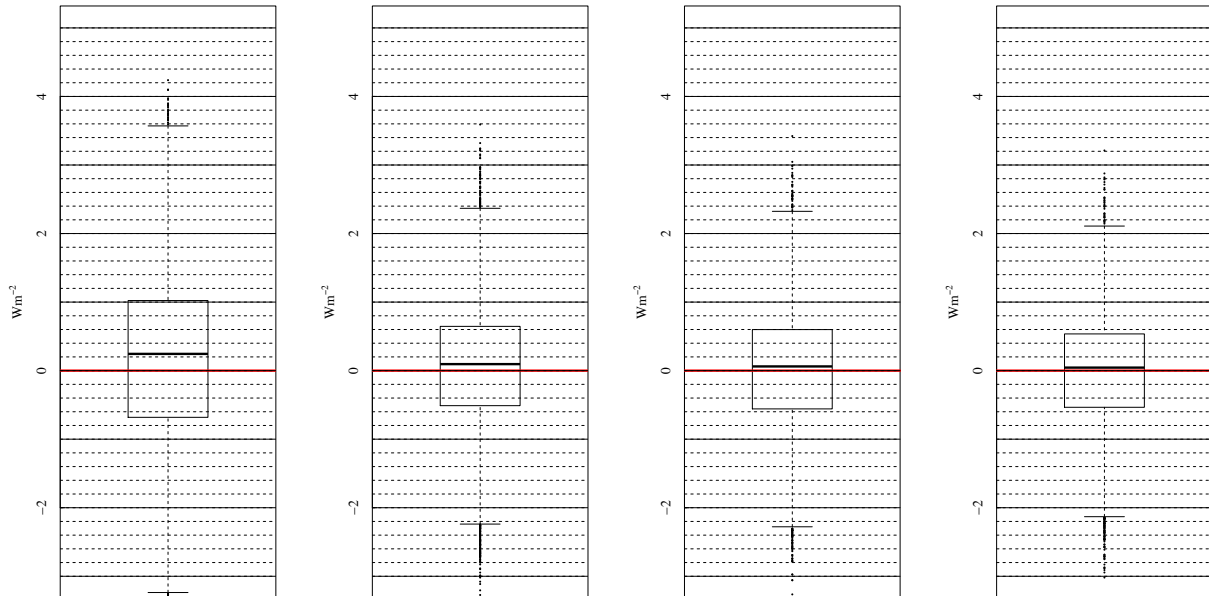
Left to Right, Albrecht Coefs, Payne Coefs, Reda Coefs, Philipona Coefs Using Philipona Stds for PIR 23215 2023 Cal



Albrecht = Albrecht and Cox (1977); Payne = Payne and Anderson (1999); Reda = Reda et al. (2002); Philipona = Philipona et al. (1995)

254

Left to Right, Albrecht Coefs, Payne Coefs, Reda Coefs, Philipona Coefs Using Philipona Stds for PIR 38805 2023 Cal



Albrecht = Albrecht and Cox (1977); Payne = Payne and Anderson (1999); Reda = Reda et al. (2002); Philipona = Philipona et al. (1995)

255

256

257 **Figure 5.** Boxplots of differences using the WRC’s Philipona et al. (1995) coefficients for the
 258 standard PIRs and calibrated PIRs to this standard using the four equations to calculate incoming
 259 IR. Top is for PIR 23215 and bottom is PIR 38805 as in Fig. 4. Compare box widths, whisker
 260 lengths, and medians.

261

262 In these comparison plots the standard used was calibrated with Philipona et al. (1995)
 263 coefficients rather than Albrecht and Cox (1977) as in Fig. 4. Similar results were obtained for

264 the other four PIRs with the best results always obtained with the Philipona et al. (1995)
265 formulation. In only one case out of the six the Payne and Anderson (1999) formula performed
266 slightly better than the Reda et al. (2002) formula (not shown).

267
268 T-tests were performed to assess differences when using non-Philipona et al. (1995) calibration
269 coefficients for all six calibrated instruments. If one assumes that there are no significant
270 differences in the calculation of IR irradiances using the Philipona et al. (1995) formula versus
271 each of the other three methods discussed, this assumption is rejected with 95% confidence in 15
272 of the 18 cases studied (six calibrated PIRs and three formulae). The three cases where the null
273 hypothesis cannot be rejected with 95% confidence are for three of the six PIRs using the Reda
274 et al. (2002) formula.

275
276 Reda et al. (2002) and Payne and Anderson (1999) did not use the measured body temperature
277 T_B in their formulae, but estimated the receiver temperature T_R using a form of Eq. (5) for their
278 particular PIR configuration. As a test we replaced T_B with T_R in the Philipona et al. (1995) Eq.
279 (3). The extremely small changes in the rightmost boxplots of Fig. 5 were imperceptible. We
280 would, therefore, suggest keeping Eq. 3 in its original form for calibration transfer.

281

282

283 **4. Precision of the PIR Standards**

284

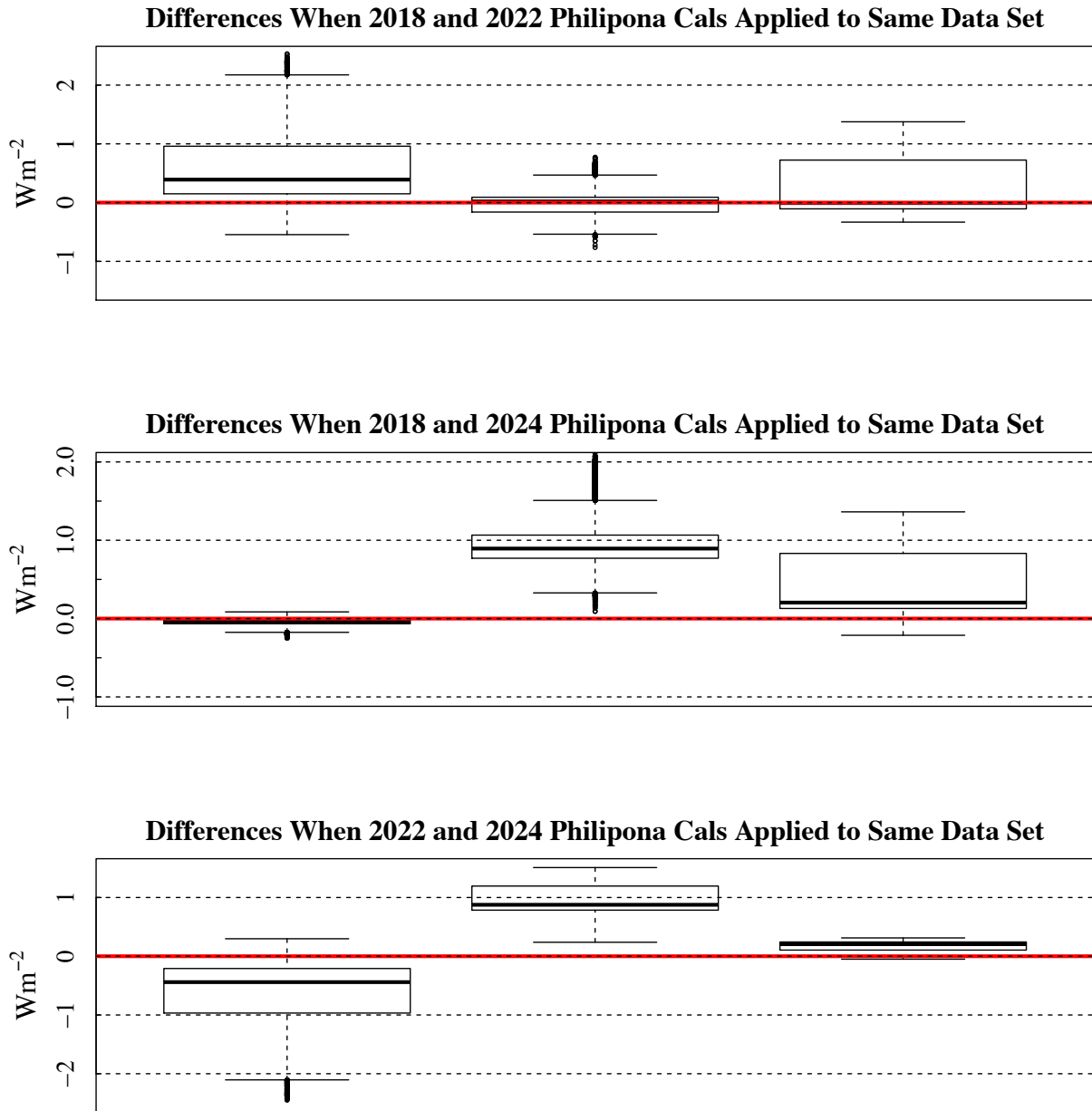
285 The calibration of our same three standard PIRs at the WRC leads to slightly different calibration
286 results. Here, the consistency and repeatability of those calibration events is assessed. The PIRs
287 that we use for standards were sent to WRC in 2018, 2022, and 2024. For each of those events,
288 coefficients for the Albrecht and Cox (1977) and Philipona et al. (1995) forms of the PIR
289 processing equation for calculating incoming IR were provided by the WRC.

290

291 Our calibration seasons typically run from Spring to early Fall. Therefore, our three standard
292 PIRs experience roughly six months of exposure to the weather each year. In Fig. 6 differences
293 from applying three sets of WRC Philipona calibration coefficients (from 2018, 2022, and 2024)
294 to the same dataset (that used for Fig. 3) are summarized. For example, calibrations from 2018
295 and 2022 were applied to the same dataset and differences in irradiance for each minute were
296 tallied and summarized in boxplots. Differences for all permutations are mostly within 1 Wm^{-2}
297 and suggest that errors from applying one of the WRC calibrations from any of the three
298 calibration years to any year would be less than the uncertainty of the WRC calibrations
299 themselves ($\sim 4 \text{ Wm}^{-2}$; <https://www.pmodwrc.ch/en/?s=wisg>). This suggests that the Eppley PIR
300 is very stable and should be suitable for monitoring long-term changes in the thermal IR.

301

302



Three Standards (31610, 32909, 32910) w/ WRC Cals from Three Different Years

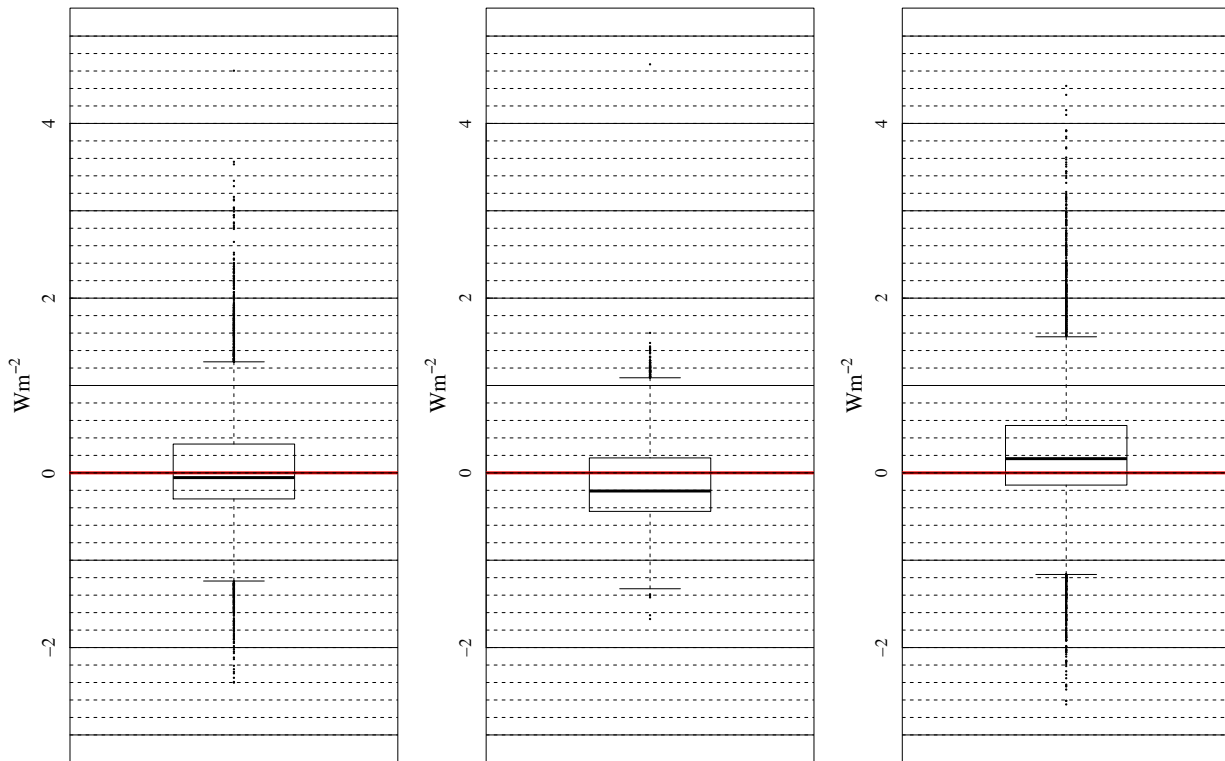
303
 304 **Figure 6.** Comparisons of three sets of Philipona et al. (1995) calibration coefficients provided
 305 by the WRC in 2018, 2022, and 2024 applied to the same data set as in Fig. 3 for the three PIRs
 306 used as standard PIRs with serial numbers in the subtitle. The medians are all within 1 Wm^{-2} and
 307 most are within 0.5 Wm^{-2} .

308
 309 In section 3 the average output of the three standard PIRs is used to derive new calibration
 310 coefficients for each test PIR. Using those new calibrations, the test instrument measurements
 311 are compared to the standard PIRs' average over the entire calibration period. For the left panels
 312 in Fig. 7 we use Philipona et al. (1995) coefficients for the standard PIRs to calibrate the three
 313 test PIRs (serial numbers shown at the top of each subplot). We apply those new calibrations and

314 subtract the results from the standard PIRs' average for each minute and summarize the
315 distribution of differences in boxplots. Therefore, the leftmost panels of Fig. 7 replicates the
316 rightmost panels of Figs. 4 and 5. This is not an independent test of the reliability of the
317 calibration because the same dataset is used for calibration and verification.

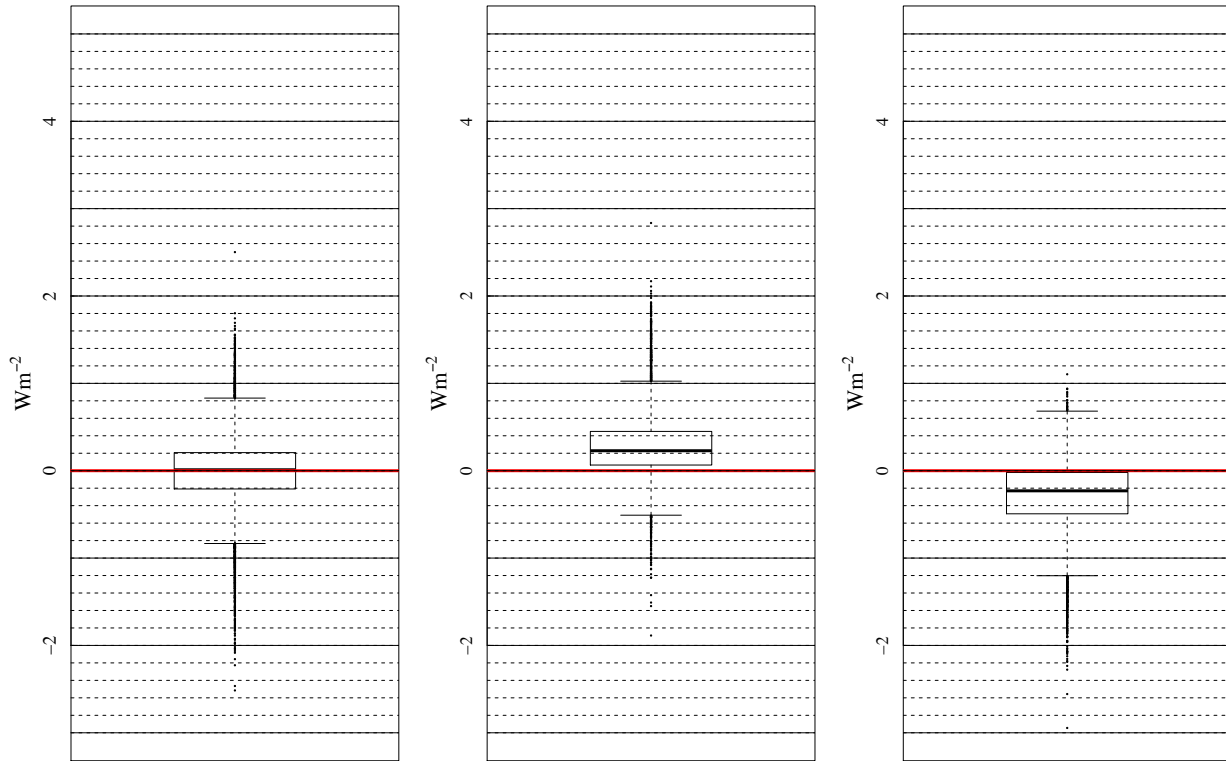
318
319 To test new calibrations with an independent dataset, the time series in Figure 3 is divided in
320 half. The middle panels of Fig. 7 use the first half of the data in Fig. 3 to derive a calibration and
321 the second half of the data to validate the new calibration against the standard PIRs' average.
322 Then, we reverse this process using the second half of the Fig. 3 data for calibrating and the first
323 half to validate. If we examine the time series in Fig. 3, it is apparent that the first half of the data
324 stream is noisier than the second half. Using the first half of the data to calibrate and applying to
325 the second half and vice versa is likely responsible for the offsets in the medians, but the offsets
326 are less than one Wm^{-2} . Note that when the less noisy data of the second half are used to validate
327 (middle boxplots) the differences have a smaller spread. When the noisier first half data
328 (rightmost boxplots) are used to validate, the differences have a larger spread. Examining the
329 top, middle, and bottom plots, there are differences inherent in the instruments themselves since
330 boxplots are not replicated from PIR to PIR. Attribution to the instruments themselves is
331 warranted because the standard PIRs and test data used for Fig. 7 were collected simultaneously.
332

Left to Right: Full Cal Period; 1st Half Used for Cal, Applied to 2nd Half; and Vice Versa for PIR 23215



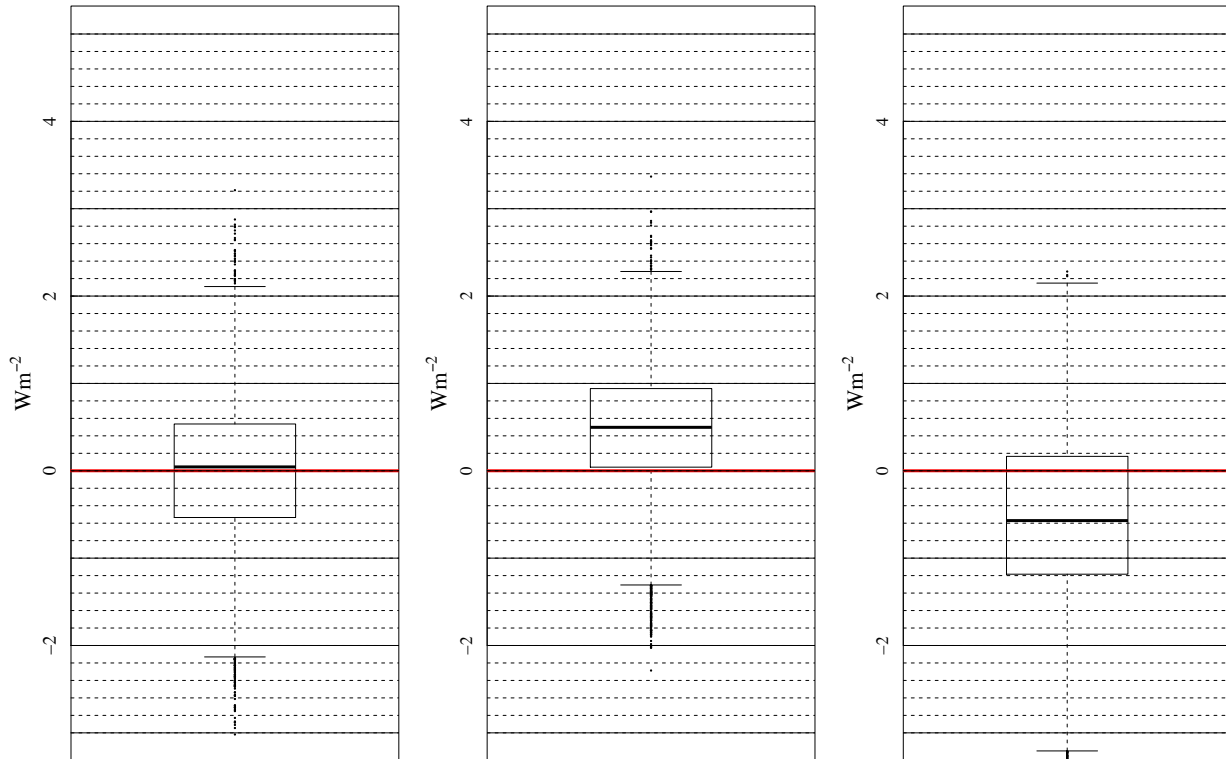
333

Left to Right: Full Cal Period; 1st Half Used for Cal, Applied to 2nd Half; and Vice Versa for PIR 28139



334

Left to Right: Full Cal Period; 1st Half Used for Cal, Applied to 2nd Half; and Vice Versa for PIR 38805



335

336 **Figure 7.** The leftmost panel uses the entire period in Fig. 3 to calibrate the named PIR and then
337 compares the calibrated PIR data to the standard PIRs' average. The middle panel uses the first
338 half of the period to calibrate and then assesses the application of those calibrations to an
339 independent data set in the second half. The rightmost panel reverses this using the second half
340 of the period for calibration and the first half for assessment.

341

342 **5. Summary and Conclusions**

343

344 In this paper we investigate four formulations for converting raw voltage and body and dome
345 temperature measurements of an Eppley pyrgeometer, model PIR, to thermal IR irradiance.
346 These methods are described in Albrecht and Cox (1977), Philipona et al. (1995), Reda et al.
347 (2002) and Payne and Anderson (1999). All are slight variations of the original formulation of
348 Albrecht and Cox (1977). Because the temperature measurements are critical to the infrared
349 calculations, we also investigated various fits that have been applied to the Steinhart-Hart (1968)
350 equation that converts thermistor-measured resistance to temperature.

351

352 Regarding the computation of thermistor temperatures, we found that fitting the manufacturer-
353 supplied table of resistance and temperature (1°C interval) to the range -50° to 50°C provides the
354 least variability as opposed to fits to shorter temperature ranges. However, differences of the fit
355 to the provided data are < 0.01°C, regardless of the range used. Based on this result, we conclude
356 that differences in thermistor temperature calculations from fits based on various temperature
357 ranges do not have a significant impact on PIR measurements.

358

359 The three standard PIRs that we use to transfer calibrations from the world standard to field PIRs
360 are calibrated frequently against the World Infrared Standard Group (WISG) at the World
361 Radiation Center in Davos, Switzerland. They are returned with calibration coefficients for the
362 Albrecht and Cox (1977) and Philipona (1995) methods, although the Albrecht and Cox
363 coefficients provided are for the shortened form of their equation (Eq. 2). Comparing the
364 application of the two methods to the standard PIRs revealed that the Philipona (1995) method is
365 more precise and less noisy than the shortened Albrecht and Cox formulation; the differences are
366 quantified in Fig. 3(b) histograms. Comparisons were also made among three distinct WRC
367 calibration results for the standard PIRs in 2018, 2022, and 2024. They showed that the three
368 standard PIRs are stable, with the calibration coefficients changing minimally between WRC
369 calibrations, and differences in irradiance calculations among applications of the separate
370 biennial calibrations are within one Wm^{-2} of each other.

371

372 Application of the four methods for converting PIR raw measurements to irradiance was
373 analyzed using six test instruments. The major conclusion is that use of the Philipona et al.
374 (1995) form, i.e., Eq. (3), consistently does the best in transferring the mean calibration of the
375 standard PIRs to field-deployed PIRs. Note that Reda et al. (2002) and Payne and Anderson
376 (1999) coefficients are not available for the standard PIRs calibrated at the WRC, which may
377 have led to some of the differences in Fig. 5. Of the six calibration comparisons, like those in
378 Fig. 5, Reda et al. (2002) calibration results were close to, but statistically different than the
379 Philipona et al. (1995) results on three of the six PIRs according to t-tests performed at the 95%
380 level. However, this agreement was found to be insignificant for the t-tests on the other three
381 PIRs.

382
 383 Given the differences in Figs. 6 and 7, it is probable that there is greater uncertainty caused by
 384 the particular atmospheric conditions under which calibrations are carried out. With the
 385 assumption that the PIR is very stable, the variations among the instruments in Fig. 6 could be
 386 subtle differences in atmospheric conditions during the three calibration sessions at the WRC in
 387 2018, 2022, and 2024. This is reinforced by the differences in Fig. 7, where independent stable
 388 (i.e., clear), and unstable (e.g., intermittent clouds) periods were used to calibrate test
 389 instruments, with differing results. Note that PIR measurements for any arbitrary weather
 390 condition are often going to have larger uncertainties than discussed here.

391
 392 The WISG, which is used for calibration at the WRC, is the current standard for broadband IR
 393 measurements. It has an uncertainty of 2.6 Wm^{-2} . Recent studies, which are summarized in
 394 Gröbner et al. (2024), further suggest that the current WISG may be low by as much as 4 Wm^{-2} if
 395 the water vapor column exceeds 1 cm, but the difference is smaller if the atmosphere is dryer
 396 approaching no difference for vanishing water vapor (see Fig. 2 in Gröbner et al., 2024).
 397 Nevertheless, a new standard for broadband IR radiation is not expected to be established until
 398 the next WMO congress in 2027 at the very earliest (Laurent Vuilleumier, private
 399 communication).

400
 401
 402 **Appendix A1**
 403

404 Fitting the manufacturer-supplied temperature (at $1 \text{ }^\circ\text{C}$ intervals) and resistance data, separately
 405 in ohms and in kilohms, led to an unexpected outcome. First, if a full cubic (i.e., non-zero
 406 coefficient for the squared term) least-squares fit of the Steinhart-Hart equation with YSI 44031
 407 data in kilohms is compared to a least-squares fit using ohms, identical fits are obtained (blue
 408 and white dashed line in Fig. 2). If the quadratic term is set to zero and the fits are made to ohms
 409 and then kilohms, we see a significant difference as shown in Fig. A1. This difference is due to
 410 numerical reasons, which are explained in the following.

411
 412 First, it must be noted that the lack of significant digits when using kilohms is not an issue
 413 because for the fits here, kilohms are computed simply by dividing the resistance value in ohms
 414 by 1000, keeping significant digits in the decimal places.

415
 416 The requirement of a quadratic term for expressing the Steinhart-Hart equation in kilohms can
 417 be demonstrated by substituting for R in Eq. (7) $1000R_k$, where R_k is in units of kilohms as
 418 shown in Eq. (A1).

$$\frac{1}{T} = a + b \cdot \ln(1000R_k) + d \cdot \ln(1000R_k)^3 \quad (\text{A1})$$

421
 422 Applying logarithm rules to Eq. (A1) results in Eq. (A2).

$$\frac{1}{T} = a + b(\ln(1000) + \ln(R_k)) + d(\ln(1000) + \ln(R_k))^3 \quad (\text{A2})$$

426 Expanding and regrouping terms in Eq. (A2) then gives Eq. (A3) through Eq. (A7).

427

$$428 \quad \frac{1}{T} = a_k + b_k \cdot \ln(R_k) + c_k \cdot \ln(R_k)^2 + d_k \cdot \ln(R_k)^3 \quad (A3)$$

429

$$430 \quad a_k = a + b \cdot \ln(1000) + d \cdot \ln(1000)^3 \quad (A4)$$

431

$$432 \quad b_k = b + 3d \cdot \ln(1000)^2 \quad (A5)$$

433

$$434 \quad c_k = 3d \cdot \ln(1000) \quad (A6)$$

435

$$436 \quad d_k = d \quad (A7)$$

437

438 Thus, when data are in kilohms an equation of the form of Eq. (A3) (i.e. full cubic) is required
 439 to match the results of Eq. (7) when data are in units of ohms. Thus, changing units of R in Eq.
 440 (7) results in a full cubic equation. This implies that a full cubic equation can be more robust
 441 than Eq. (7) when fitting data where units other than ohms are used for R . It also demonstrates
 442 that it is possible to change units for R in Eq. (7) analytically using the substitution process
 443 shown above rather than refitting if desired.

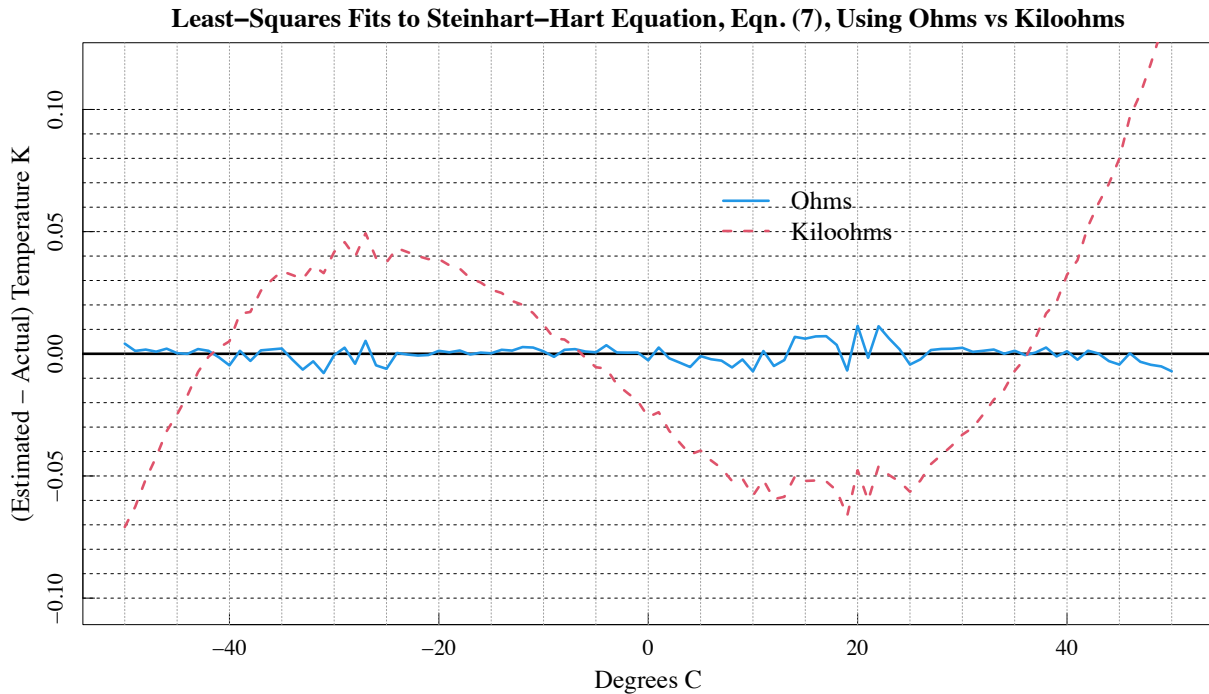
444

445

446

447

448



449

450 **Figure A1.** Steinhart-Hart equation (i.e., no quadratic term) fit to ohms (blue solid line) versus
 451 kilohms (red dashed line).

452

453

454 *Code availability.* Codes used to generate the results in this paper were original functions written in the
455 programming language R and are available by contacting joseph.michalsky@noaa.gov.

456 *Data availability.* Data can be made available by contacting joseph.michalsky@noaa.gov.

457 *Author contributions.* JJM did most of the analyses, drafted the paper, and produced the figures. JAA
458 provided the World Radiation Center calibrations and much useful discussion of the results. EH provided
459 the experimental data from the calibration table used for these analyses. BRS did the analysis for and
460 wrote the Appendix. All authors read and offered corrections to parts of the manuscript.

461

462 *Competing interests.* The contact author has declared that none of the authors has any competing interests.

463

464 *Acknowledgments.* The authors would like to thank Kathy Lantz for a careful reading of this paper.
465 Christopher Cox and another reviewer, who wished to remain anonymous, refereed the paper that
466 substantially improved the final result. Julian Gröbner performed the calibration of our standards at
467 PMOD and added useful information in a community comment. Bruce Forgan privately sent comments
468 on the paper that were appreciated.

469

470 *Financial support.* This research has been supported by the Global Monitoring Laboratory of the National
471 Oceanic and Atmospheric Administration.

472

473

474

475

476

477 **References**

478

479 Albrecht, B. and Cox, S. K.: Procedures for improving pyrgeometer performance, J. Appl.
480 Meteorol., 16, 188-197, [https://doi.org/10.1175/1520-0450\(1977\)016<0190:PFIPP>2.0.CO;2](https://doi.org/10.1175/1520-0450(1977)016<0190:PFIPP>2.0.CO;2),
481 1977.

482 Gröbner, Julian, Thomann, Christian, Reda, Ibrahim, Turner, David D., Feierabend, Moritz,
483 Monte, Christian, McComiskey, Allison, and Reiniger, Max: Traceability of surface longwave
484 irradiance measurements to SI using the IRIS radiometers, AIP Conference Proceedings, 2988,
485 070001, <https://doi.org/10.1063/5.0183304>, 2024.

- 486 McArthur, L.: Baseline Surface Radiation Network (BSRN) - Operation Manual Version 2.1,
487 Ontario, Canada, WMO, p. 68, [hdl:10013/epic.52032](https://doi.org/10.10013/epic.52032), 2005.
- 488 Payne, R.E. and Anderson, S.P.: A new look at calibration and use of Eppley precision infrared
489 radiometers. Part II: calibration and use of the woods hole oceanographic institution improved
490 meteorology precision infrared radiometer, J. Atmos. Ocean. Tech., 16, 741-751,
491 [https://doi.org/10.1175/1520-0426\(1999\)016<0739:ANLACA>2.0.CO;2](https://doi.org/10.1175/1520-0426(1999)016<0739:ANLACA>2.0.CO;2), 1999.
- 492 Philipona, R., Frohlich, C., and Betz, C.: Characterization of pyrgeometers and the accuracy of
493 atmospheric longwave, Appl. Optics, 34, 1598-1605, <https://doi.org/10.1364/AO.34.001598>,
494 1995.
- 495
496 Reda, Ibrahim, Hickey, John R., Stoffel, Tom, and Myers, Daryl: Pyrgeometer calibration at the
497 National Renewable Energy Laboratory (NREL), J. Atmos. Sol.-Terr. Phy., 64, 1623-1629,
498 [10.1016/S1364-6826\(02\)00133-5](https://doi.org/10.1016/S1364-6826(02)00133-5), 2002.
- 499 Steinhart, John S. and Hart, Stanley R.: Calibration curves for thermistors, Deep-Sea Res., 15,
500 497-503, [https://doi.org/10.1016/0011-7471\(68\)90057-0](https://doi.org/10.1016/0011-7471(68)90057-0), 1968.